

Chapter 3

Scanning Tunneling Microscopy: Principle and Instrumentation

Scanning tunneling microscopy (STM) has been proven to be an extremely powerful tool for studying the electronic structures of solid-state systems. The STM topographic images, assisted by other surface analysis techniques with chemical specificity, lead to the structural determination of clean and adsorbate-covered surfaces. For example, the first atomically resolved STM image in history confirmed the Si(111) 7×7 surface reconstruction [128] and identified Takayanagi's dimer-atom-stacking-fault model [129] as the correct Si(111) 7×7 surface structure. Combining scanning tunneling microscopy with spectroscopy, a number of beautiful experiments were carried out, *e.g.*, to visualize the standing wave pattern of the two-dimensional surface state electrons in an artificial quantum corral [130, 131], to provide the first direct spectroscopic signature of the Kondo resonance of an isolated magnetic impurity in a non-magnetic host [132], and to map out the electronic density of states inside a single vortex core of the Abrikosov flux lattice for a conventional type II superconductor [133, 134]. Furthermore, spatially resolved tunneling spectroscopy gave invaluable insights into open questions in the physics of strongly correlated electronic systems, such as the correlation between charge ordering and the metal-insulator transition in magnetic manganites [135] and the various ordering phases in high-temperature cuprate superconductors. In this chapter, we summarize the operating principles of scanning tunneling microscopy/spectroscopy and then present our development of a magnetic-field-compatible, cryogenic, variable-temperature STM for the study of cuprate superconductors.

3.1 Brief review

Scanning tunneling microscopy (STM) was invented by Binnig and Rohrer in 1981 [136, 137]. By integrating scanning capacity into vacuum tunneling capability, STM enables us to image the surfaces of conducting samples and study their local electronic properties down to atomic scales. Useful information on the physics of STM, general design and instrumentation principles, and the extension to other scanning probe techniques can be found in references [138, 139].

The essential components of an STM include a sharp probing tip; a piezoelectric scanning unit, which controls the vertical and lateral movement of the tip; a coarse positioning unit, which brings the tip-sample separation to within the tunneling range ($\sim \text{\AA}$); a vibration isolation stage; and a set of electronics, which detects the small tunneling current ($\sim 10 \text{ pA} - 1 \text{ nA}$), controls the piezo-tube scanner with feedback, and drives the coarse positioning [Fig. 3.1].

Figure 3.1 is a schematic diagram of our STM system. The arrows denote the travel direction of the commands and the electronic signals. For instance, the STM digital feedback controller takes the output signal from the current pre-amp, compares the signal level with the preset value, calculates the response according to the user-defined feedback parameters, and sends the feedback voltage through an analog to digital converter to the high-voltage amplifier, which then magnifies the input signal to drive the piezo scanner. On the one hand, the controller communicates with the computer to change the experimental settings, such as the bias voltage, the tunneling current set point, the scanning range, scanning speed and the proportional/integral (P-I) gain for the feedback algorithm. On the other hand, it also transfers the feedback signal and tunneling current signal back to the computer to generate topographic images and tunneling spectra.

To initiate the tunneling process, the STM tip is brought to within several angstroms from the sample surface by the coarse approach walker. Applying a bias voltage between the sample and the tip electrode gives rise to a quantum mechanical tunneling current. Since the tunneling probability amplitude is an exponential function of the tip-sample separation, the value of the tunneling current is extremely sensitive to the sample surface corrugation. For instance, given a work function $\sim 1 \text{ eV}$, a decrease in separation of 1 \AA increases the tunneling current by a factor of ~ 3 . During topographical

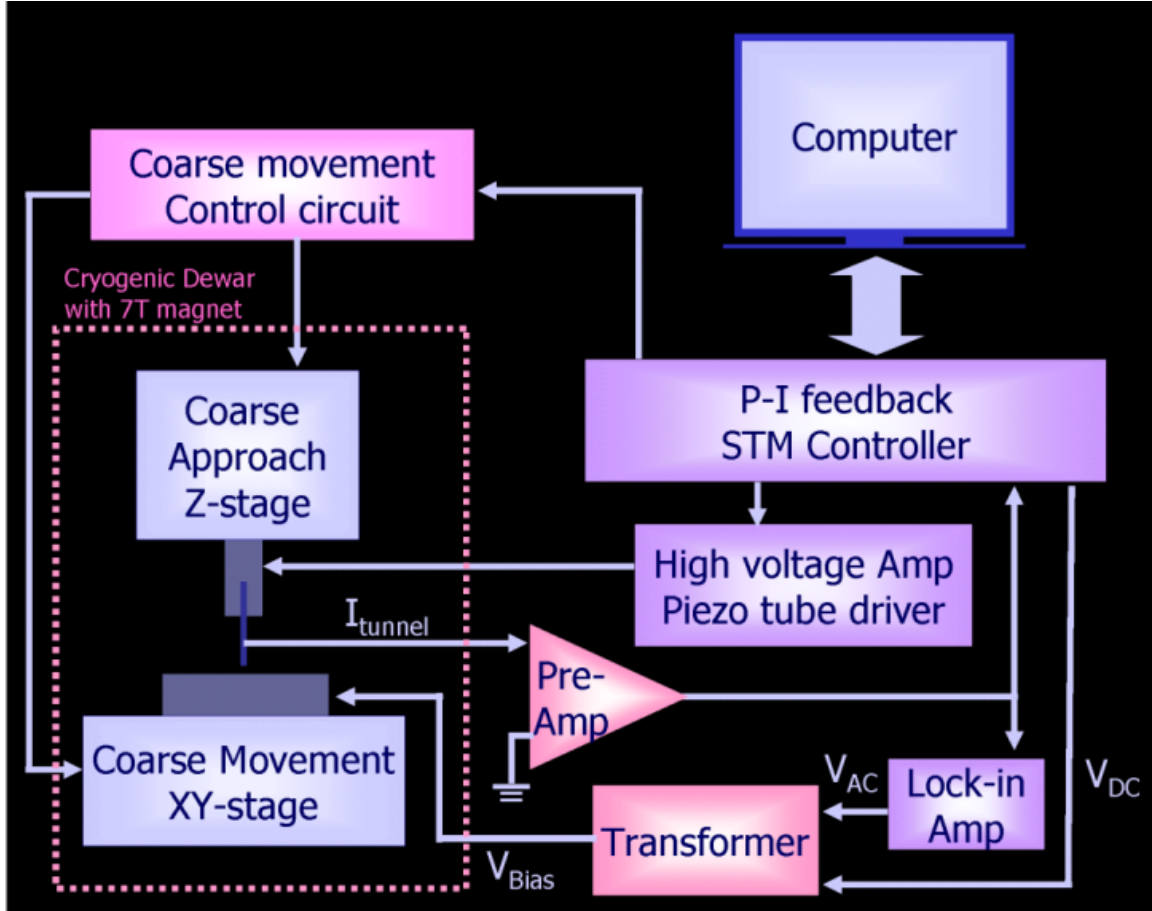


Figure 3.1: Block diagram of an STM system. The arrows denote the traveling direction of the commands and the signals. The STM head is schematically represented by the coarse approach z -stage and the sample translation xy -stage. The feedback controller, the current pre-amplifier, the high-voltage amplifier for the scanner, the high-voltage control circuit for coarse approach and the Stanford Research Systems lock-in amplifier (SR-830) form a complete set of electronics for STM control and data acquisition. The coarse movement control circuit includes a Physik Instrumente E-420 high-voltage amplifier and a homemade sequential triggering circuit [Fig. 3.2].

image scanning, by keeping the tunneling current constant with the feedback adjustment, the output voltages from the feedback loop to the z -electrode of the piezo tube are converted to deduce the vertical position of the tip as a function of its lateral position, $z(x, y)$. This is called constant-current topographic imaging.

Via constant-current imaging, we can identify the feature of interest and zoom in to investigate its local electronic structure, more specifically, its local density of states (LDOS), with the tunneling spectroscopy capability. As derived in Chapter 2, by studying the differential conductance (dI/dV) in a planar-junction-type of tunneling experiment, the averaged DOS of the sample is extracted. To

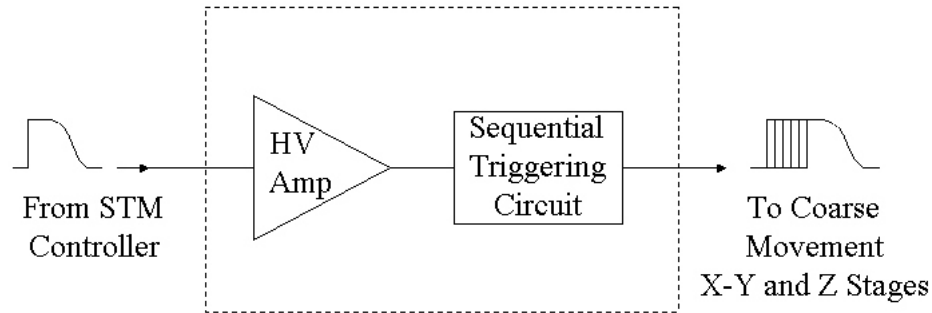


Figure 3.2: Schematic diagram of the STM coarse movement control unit.

obtain the spatially resolved LDOS, we measure the tunneling spectra point by point on target areas. During a set of scanning tunneling spectroscopy measurements, a constant tip-sample separation is first established by fixing the set-point current at a given bias voltage. Next, the feedback is turned off and a small sinusoidal modulation is added to the DC bias voltage. The resulting current modulation ($\propto dI/dV$) is then read off from a lock-in amplifier, into which the tunneling current signal from the current pre-amplifier is fed. We record the output signal from the lock-in amplifier as a function of the DC bias voltage to generate a tunneling spectrum $\frac{dI}{dV}(\vec{r}, V)$, and hence the LDOS. By taking dI/dV along a line or by taking a two-dimensional dI/dV map, changes in LDOS around a impurity, across a step-edge, or among grains with different crystalline orientations can be revealed and compared with theoretical predictions.

3.2 Instrumentation of a cryogenic STM

For an STM to perform spectroscopy measurements with atomic scale resolution reliably, several instrumentation challenges must be overcome. The coarse approach mechanism has to bring the probing tip smoothly into the tunneling range ($\sim 5 \text{ \AA}$) without crashing onto the sample. Secondly, the tip-sample separation has to remain constant to within $\sim 0.1 \text{ \AA}$ throughout any measurement. That is to say, mechanically the design of the STM should be rigid enough to prevent vibrational couplings from changing the tip-sample distance. The mechanical disturbance from the environment and acoustic vibrations should be decoupled as much as possible from the STM head.

Electronically, tunneling currents generally range from \sim pA to \sim nA. To avoid artifacts in tunneling spectra due to noise contamination, the electronics must be well shielded from ambient electromagnetic interference. Ground loops must be avoided, and cross-talk between the high-voltage piezo driving signals, the temperature controller output and the low-level tunneling/bias signals need be minimized.

Thermally, to track the evolution of cuprate electronic properties from the low-temperature superconducting state to above the transition temperatures, it is required that the STM system have good thermal stability, low thermal drift, good thermal isolation when operating at high temperatures, and sufficient cooling power to attain low base temperatures. Furthermore, problems associated with gas desorption and sample contamination at elevated temperatures must be addressed.

This section describes the design of our STM head and the cryogenic probe, and the measures taken to counter the aforementioned technical challenges under a modest budget. Other information related to the preparation of STM tips, the calibration of the shear piezos and the piezo-tube scanner, and the STM images on highly ordered pyrolytic graphite and gold samples for calibration purposes is given in Appendix B.

3.2.1 STM head

The STM built as part of this thesis work is intended to operate at variable cryogenic temperatures, in high vacuum, and in high magnetic fields. To compensate for the undesirable noisy environment of the lab and to fit the system into a 3" bore magnet, we adopted Pan's STM design [140, 141] with some variation because this design ensures a compact, rigid, high-vacuum and high-field-compatible STM head. There is a variety of distinct STM designs. In general, they differ in how the coarse approach is implemented and in their rigidity against vibrations. Pan's design employs a modified "stick-slip" coarse approach mechanism that exploits the friction between parts to hold the unit against vibrational noise coupling.

The STM head [Fig. 3.3] consists of a Macor¹ housing (1), six shear-piezo stacks² (2) with alumina

¹A machinable ceramic manufactured by Corning Inc.

²0.040" thick EBL-2 shear piezos purchased from Staveley Sensor.

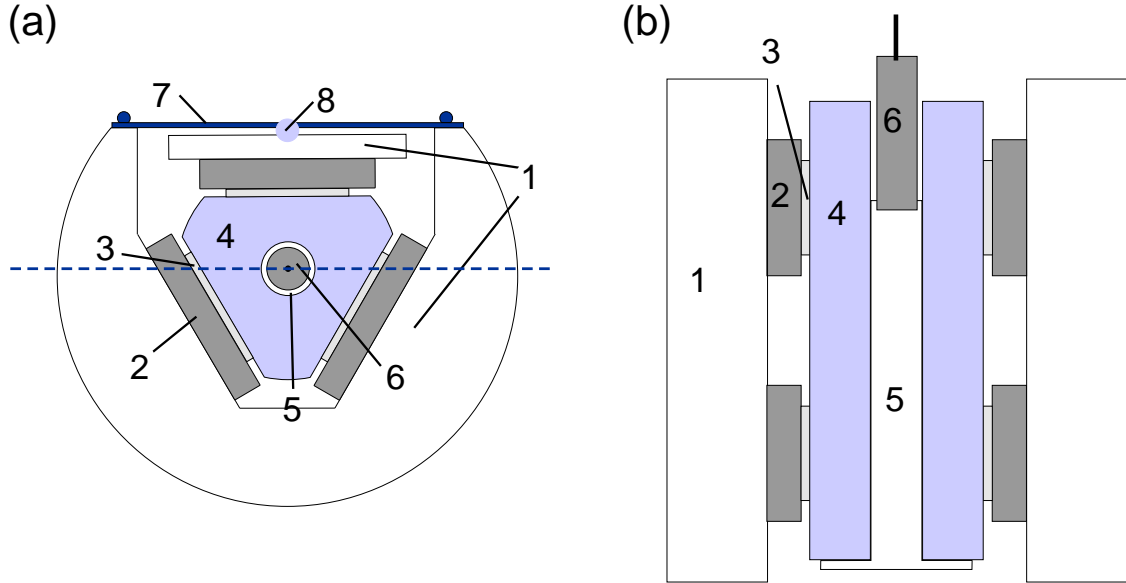


Figure 3.3: Schematics of the STM head, not to scale. (The sample holder is omitted.) (a) Top view. (b) Side view along the cut denoted by the dotted line. (1) Macor body, (2) shear-piezo stacks, (3) alumina plate contacts, (4) sapphire prism, (5) Macor insert of the scanning unit, (6) piezo-tube scanner, (7) Be-Cu spring plate, (8) sapphire ball bearing.

plate contacts³ (3), a sapphire prism⁴(4) that carries the scanning unit, and a Be-Cu spring plate (7). The scanning unit is made of a Macor insert⁵(5), a piezo-tube scanner⁵(6), and a metallic tip holder. The metallic tip holder is attached to the center of the piezo-tube scanner, and the scanner is glued to the top of the Macor insert with Torr Seal.⁶ The Macor piece fits tightly to the central hole of the sapphire prism, and the scanning unit is locked to the sapphire with screws and TorrSeal. By pressing down a 1/8" diameter sapphire ball (8) against the top Macor block (1), the Be-Cu spring plate (7) holds the sapphire prism firmly between six piezo stacks. All of the materials chosen are non-magnetic and ultra-high-vacuum compatible. The overall dimension of the STM head is about 1.5" in diameter and 2" in height.

The operating principle of the shear-piezo motor is shown in Fig. 3.4. To move the sapphire one step forward, we apply six sharp high-voltage steps sequentially to the six shear-piezo stacks, so that the piezos move backward one stack at a time, while the other stacks hold the sapphire

³0.020" thick Superstrates manufactured by Coors Ceramic Company.

⁴Purchased from Insaco, Inc.

⁵0.020" thick, 0.125" OD, EBL-2 piezo tube purchased from Staveley Sensor.

⁶Purchased from Varian Inc.

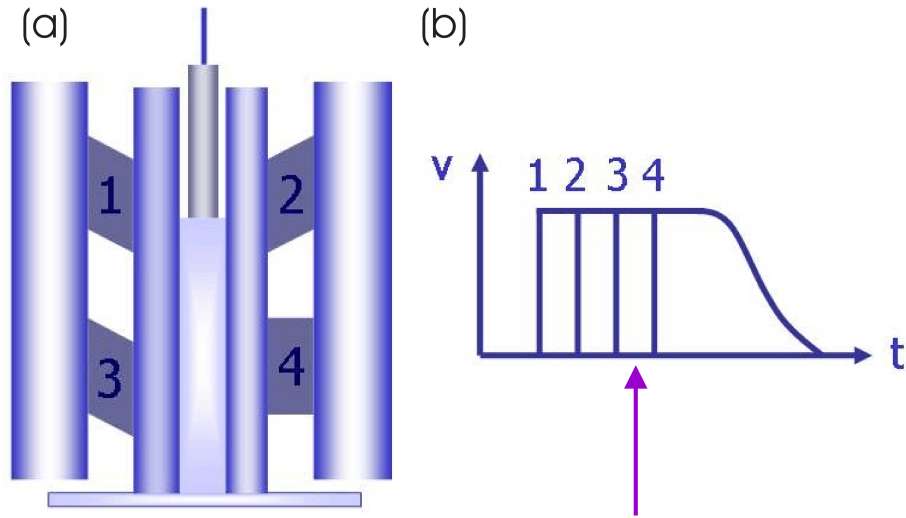


Figure 3.4: Principle of the coarse approach mechanism. (a) Snapshot of the configuration of the piezo stacks during a coarse movement cycle. (Only four of the six stacks are shown.) (b) Voltage waveform applied to the piezo stacks as a function of time. The arrow indicates when the snapshot is taken.

prism steady by friction. After every piezo stack is displaced from its resting position, we slowly decrease the applied voltages to zero. As a result, the six piezo legs simultaneously relax back to their neutral positions and, through friction, bring the prism forward by one step. The size of each step is determined by the shear-coefficient of the piezos ($\sim 8 \text{ \AA}/\text{V}$ at room temperature, and $\sim 1.5 \text{ \AA}/\text{V}$ at 4.2 K), the applied voltages and the number of piezos per stack. Typically, at room temperatures, one coarse step is about $0.4 - 0.8 \text{ }\mu\text{m}$ with an applied voltage between $150 - 300 \text{ V}$, while the vertical probing range of the piezo-tube is over $1.0 \text{ }\mu\text{m}$, larger than the coarse approach step size. Therefore, by applying feedback voltages to the piezo-tube, we can safely advance the tip forward without crashing onto the sample.

This design is superior in its stability against external mechanical perturbations. The sapphire prism and the tip it carries are held steady by friction between the alumina contacts and the prism. The strength of the friction can be adjusted by varying the curvature of the thin Be-Cu spring. Therefore, there is very little relative motion between the Macor body and the tip. Furthermore, after each step is completed, all piezos return to their neutral positions. Thus, no voltage is needed to hold the prism in place, and the vibrational noises transmitted through the voltage noises applied

to the piezos are eliminated.

One additional advantage of the design is its stability against thermal expansion. The STM head is designed to be concentric with the tip and sample located at the center. Therefore, it minimizes thermal drifting and enhances the STM performance at variable cryogenic temperatures. Besides, the Be-Cu plate is heat-treated to retain its springing strength during thermal cycling. Therefore, the rigidity of the STM head is guaranteed throughout the temperature range from 4K to ~ 100 K.

3.2.2 STM electronics

The STM control and data acquisition electronics consist of a high-gain low-noise current pre-amplifier⁷, a digital P-I feedback controller⁸, a set of high-voltage amplifiers that control the piezo-tube scanner, a high-power high-voltage amplifier⁹ and a homemade triggering circuit that controls the coarse approach piezo motor. A block diagram of the STM is given in Fig. 3.1.

The low-noise current pre-amp has a variable gain up to 1×10^{12} . We operate the pre-amp mostly at a gain of 1×10^9 for data acquisition and at 1×10^6 for field-emission tip cleaning. When operated at 1×10^9 , the output voltage noise is below 4 mV (peak-to-peak), equivalent to a ≤ 4 pA (peak-to-peak) input referred noise.

The STM digital feedback controller [Fig. 3.5] is built around two 32-bit floating point digital signal processors.¹⁰ One of them is designated for the feedback control and the other for imaging, data collection, data buffering, and data transfer. There are four 20-bit digital-to-analog converters (DAC's) for the high-voltage scanner control and the low-level sample bias voltage, and there are five 16-bit 100 kHz analog-to-digital converters (ADC's). The tunneling current signal from the pre-amp is connected to one of the ADC's with programmable gain (2 – 16) and a digital filter (2 – 20 Hz). The remaining four auxiliary analog input ports can be used to perform simultaneous data acquisition, *e.g.*, from the lock-in amplifier output during constant-current imaging.

To coordinate the coarse approach with the fine scanner control, there is an additional DAC that

⁷Model 1211 from DL Instruments.

⁸Purchased from Custom Vacuum System.

⁹E-420 from Physik Instrumente.

¹⁰ADSP-21062—SHARC manufactured by Analog Devices.

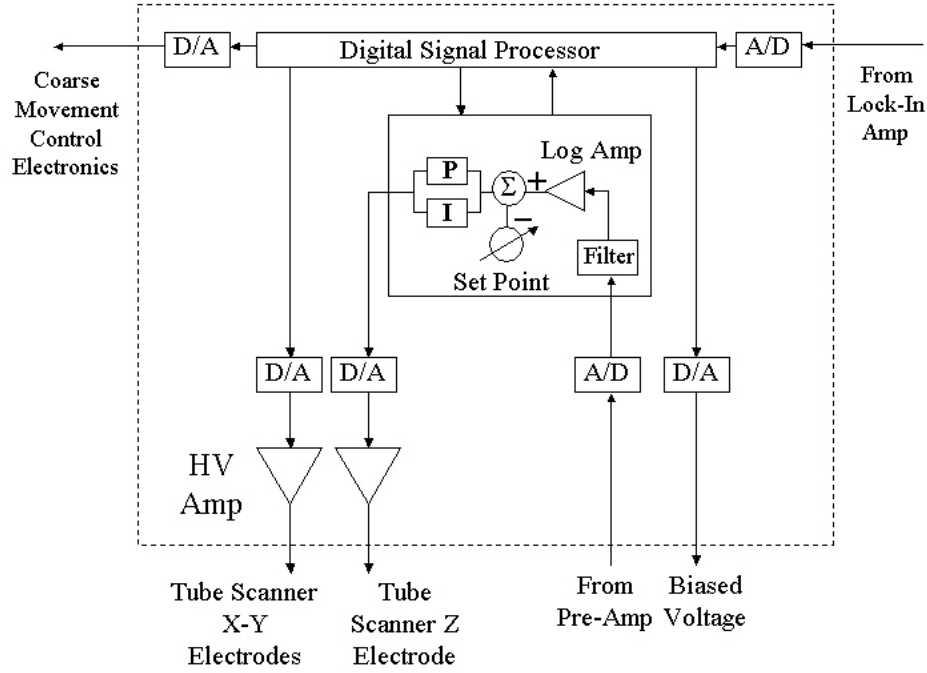


Figure 3.5: Schematic of the proportional/integral gain (P/I) digital STM feedback controller.

generates the triggering waveform for the coarse movement control of the shear-piezo walker. When the tip is brought within the tunneling range, under a constant sample bias voltage, the controller takes the amplified current signals from the pre-amp, performs the P/I feedback algorithm and, finally, outputs a voltage signal to the z -electrode of the piezo-tube to maintain a constant tunneling current. The five built-in monolithic high-voltage amplifiers (± 220 V) drive the scanning tube to manipulate the raster and vertical motion while the ADC's and the second digital signal processor record the data and transfer them to the computer.

Another important component of the STM electronics is the coarse movement control electronics. It includes a high-voltage high-power amplifier purchased from the Physik Instrumente (E-420) and a homemade sequential triggering circuit that gates the high-voltage output from E-420 to the coarse approach piezo stacks [Fig. 3.2]. For the slip-stick coarse approach mechanism to function properly, we need the capability of charging the piezo stacks (~ 4 nF each) to 400 V within $1 \mu\text{s}$ [Fig. 3.4] in order to overcome the huge static friction between the sapphire prism and the piezo stacks. Since no commercial high-voltage amplifier could provide such a large instantaneous current, we add to the

triggering circuit two large capacitors¹¹ as charge reservoirs to supply additional currents in each pulse cycle.

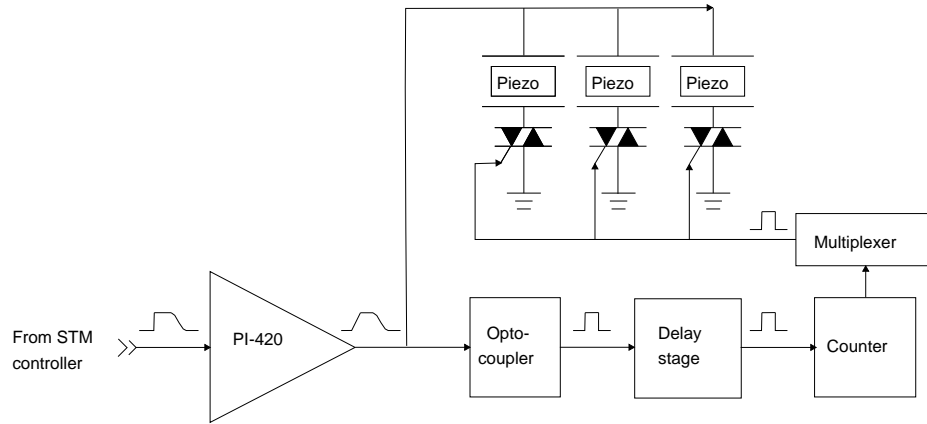


Figure 3.6: Schematic diagram of the sequential triggering circuit. (Only three of the six ports are shown for simplicity.) The high-voltage signal from E-420 is decoupled from the low-level digital circuitry via an optocoupler. The clock frequency of the counter that controls the sequential charging interval is set by a variable resistor. The oscillator consists of two inverters and two capacitors in addition to the resistor.

The schematics of the high-voltage triggering circuit is shown in Fig. 3.6. During each cycle, the delay stage receives a trigger signal from the optocoupler and waits until the capacitors are fully charged before it sends a pulse to the timer. After receiving the pulsing signal, the timer counts from one to eight with a user-defined time interval and sends the output number to the multiplexer. Then, the multiplexer sends a triggering signal to the gate electrode of the corresponding high-voltage-sensitive-gate triac to charge up the individual piezo stack. Consequently, the piezos are activated sequentially with the specified time interval and a very high instantaneous current. In our design, the time interval and the delay are set by variable resistors to be $\sim 50 \mu\text{s}$ and $\sim 0.5 \text{ ms}$, respectively, while the duration of the entire pulse is programmed to be $\sim 3 \text{ ms}$.

Overall, the speed of the coarse approach is limited by the bandwidth of the feedback to $\sim 1 \text{ step/sec}$. At room temperatures, it takes less than an hour to move the tip $\sim 3 \text{ mm}$ forward into tunneling range. At helium temperatures, because of the reduced piezo coefficient and the increased friction between the sapphire prism and the alumina contacts, it usually takes overnight to reach the tunneling range.

¹¹2 μF , rated at 630 V, purchased from Digi-Key Corporation

3.2.3 Cryogenic probe and dewar

The STM probe [Fig. 3.7] used in this thesis work is adapted from an old probe made for a gas-cooled, solenoid-driven STM head. The backbone of the probe is a 1 in. diameter, 3.5 ft. long thin-wall stainless steel (SS) tubing (6), situated in a 2.5 in. diameter stainless steel vacuum can (5). A charcoal pump (8) is installed at the bottom of the vacuum can to absorb the residual gas from any virtual leaks of the STM head at low temperatures. Otherwise, the high-voltage-driven coarse approach may cause undesirable discharge and damage the piezo motor. For the same reason, we have to eliminate the use of helium exchange gas for cooling to protect the STM head. At room temperature, we routinely reach $\leq 5 \times 10^{-6}$ torr by using a turbo pump without having to bake out the charcoal. When the probe is immersed in liquid helium or liquid nitrogen, the pressure is maintained to below the scale of our ion gauge ($\leq 10^{-8}$ torr) because of the extra pumping power received from the charcoal pump.

In the absence of exchange gas, the original design of the probe is not able to provide enough cooling power, and the thermal load from the room temperature end becomes detrimental. We address this problem by reducing the thermal radiation and conduction and by increasing the thermal link to the helium bath. For example, Be-Cu springs (3) are attached to the bottom two stainless steel (SS) baffles (2) around the SS backbone tubing to ensure that the baffles are in good contact with the vacuum can and, hence, the liquid helium bath. In addition, ten Cu baffles (1) are added to the center of the SS tubing to reflect the thermal radiation down the tubing. These two measures combine to improve the radiation shielding, establish a uniform thermal gradient along the probe, and shunt the thermal conduction through the backbone tubing.

Next, we minimize the thermal conduction of the electrical wires. For example, 36 AWG manganin wires,¹² known to have low thermal conductivity are used for wiring the piezo stacks, piezo-tube scanner, and the copper foil heater¹³ and 36 AWG phosphor bronze Quad-Twist wires.¹⁴ are used for the Cernox temperature sensor¹⁴ The bias voltage lead is a 4'' long stranded 304 SS flexible

¹²Purchased from the California Fine Wire Company.

¹³Purchased from Minco Co.

¹⁴Purchased from Lakeshore Cryotronics, Inc.

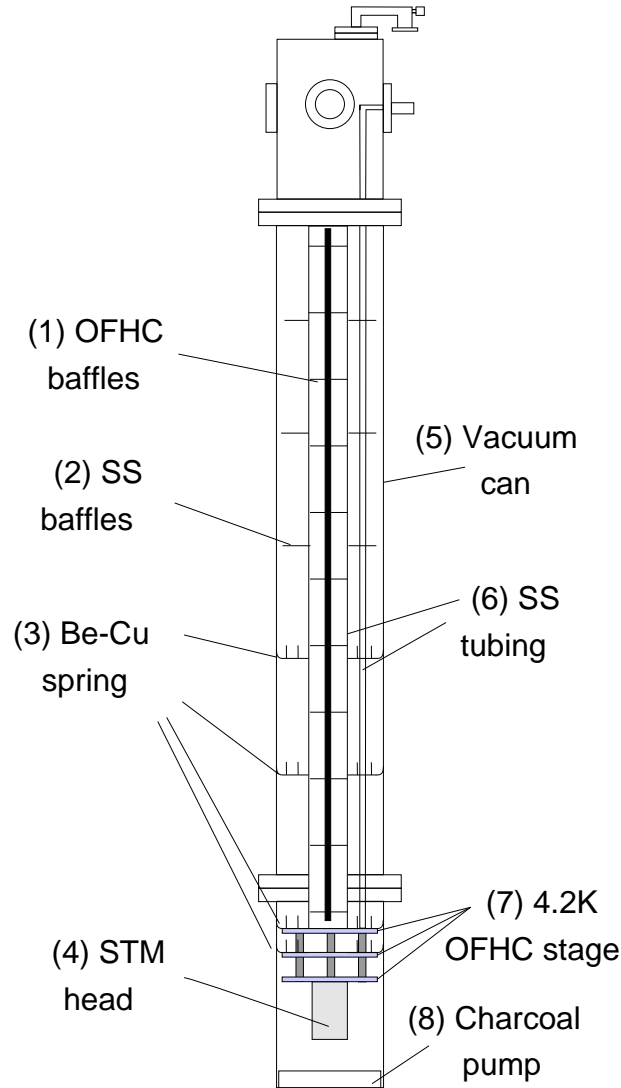


Figure 3.7: STM cryogenic probe. (Not to scale.)

mini-coaxial cable¹⁴ with a negligible thermal load ($\ll 1$ mW).

The remaining heat load comes from the thermal conduction through the lead carrying the tunneling current. To reduce the coupling of vibrational noises through the microphone effect, we use a 0.141" diameter rigid coaxial cable for the tunneling signals. Ideally, the 20 mil semi-rigid mini-coax from Lakeshore is a better choice because of its low thermal conduction. However, it is difficult to attach SMA connectors to the cable without partially pinching its extremely thin insulating layer. As a result, the cables always come with a partial short on the order of $\sim 10^{10} \Omega$,

unacceptable for any high-impedance tunneling experiment. Thus, we compromise on the thermal performance and settle for a 3.5' long 0.141" coaxial cable with Cu inner conductor and SS outer shielding.

To reduce the heat leak through the inner conductor of the coax, we replace the bottom section of the cable with a 0.5' long 36 AWG manganin wire, and the resulting thermal load is suppressed to below 1 mW. Next, we tackle the ~ 6 mW heat leak through the SS outer conductor by thermal anchoring it with four gold-coated copper wires to the bottom radiation baffle. One end of the wires is wrapped around the manganin section of the coaxial cable and held in place with VGE-7031 varnish, while the other end is firmly attached to the bottom baffle. For more than 5 liters of liquid helium left in the dewar, the estimated temperature difference across the copper wires is ~ 70 K, and therefore the thermal anchoring provides at least ~ 10 mW of cooling power, sufficient to compensate for the heat load through the SS outer conductor.

To reduce the heat load further, we anchor the wires of the piezo motor, the piezo-tube scanner, and the temperature sensor to two 4.2 K stages made of oxygen-free high-conductivity copper (OFHC) before connecting them to the STM head. In addition, we pass the bias voltage and the tunneling current leads through the cryogenic microwave powder filters [142] attached to the bottom OFHC stage. Several Be-Cu spring contacts (3) firmly establish the thermal link between the 4.2 K stages and the outer can, thus providing enough cooling power for the entire STM head. After the installation of baffles and heat sinks, base temperature significantly improves from ~ 30 K to ~ 9 K.

The Oxford dewar housing the STM probe holds up to ~ 35 liters of liquid helium. It comes with a 3" bore superconducting magnet. The upper section of the magnet leads are thin-wall brass tubing with copper wires soldered along their circumference, which extend to the bottom magnet. These leads are designed to be in direct contact with the helium bath and are not retractable from the flange of the dewar. Consequently, the boil-off rate of liquid helium reaches ~ 10 liters per day, which corresponds to 3–4 days of experiment between refilling.

3.2.4 Noise reduction

For an STM to achieve its best performance, noise contamination must be minimized. For example, in the constant-current topography mode, we need to restrict the lateral vibrational noise coupling to $\leq 0.5 \text{ \AA}$ and the vertical vibrations to $\leq 0.1 \text{ \AA}$ in order to have good atomic resolution. In the spectroscopy mode where feedback is disabled, the rigidity of the STM head against vibrations is even more crucial. A disturbance of $\sim 1 \text{ \AA}$ in the vacuum tunneling gap typically would cause the tunneling current to fluctuate by a factor of ~ 5 , so it would wash out whatever information encoded in the spectrum. Thus, we first address the reduction of mechanical coupling to the lab environment and acoustic vibrations before turning to the issue of minimizing electrical interference.

The STM lab is located in the sub-basement where the floor vibration is presumably the least severe. Nevertheless, as we set up the accelerometer¹⁵ and physically measure its noise spectrum, several sharp resonant peaks below 100 Hz are found [Fig. 3.8(a)], among which noises of $\sim 50 \text{ Hz}$ are the most pronounced.¹⁶ To suppress the coupling to these resonance modes, the dewar holding the STM probe is bolted to a 3'' thick aluminum plate and placed on a four-post Newport air damper, which serves as a low-pass filter of the floor vibrations. Additional lead bricks and lead shot bags are placed around the table to increase the loading and suppress the corner frequency of the air damper. When the table is inflated, the transmitted vibrational noises are suppressed to less than 2% of its original amplitude at the resonant frequencies [Fig. 3.8].

Another type of vibrational noise is transmitted through acoustic coupling. The acoustic noises that plague the STM system mostly come from the room ventilation motors. This type of low-frequency noises are generally difficult to remove because they either drive the plaster wall or indirectly couple through the ceiling to vibrate the whole lab. In our case, the two main sources are the ventilation pipeline mounted directly to the lab side wall and another big motor facing the lab entrance.

The following two measures are taken to contain these noises: the maximization of sound absorption and the minimization of sound transmission. We cover all of the side walls of the STM lab

¹⁵ENTEK 9200L accelerometer purchased from Rockwell Automation.

¹⁶Data in Fig. 3.8 were taken by Timothy Ward during his SURF study at Caltech in the summer of 2004.

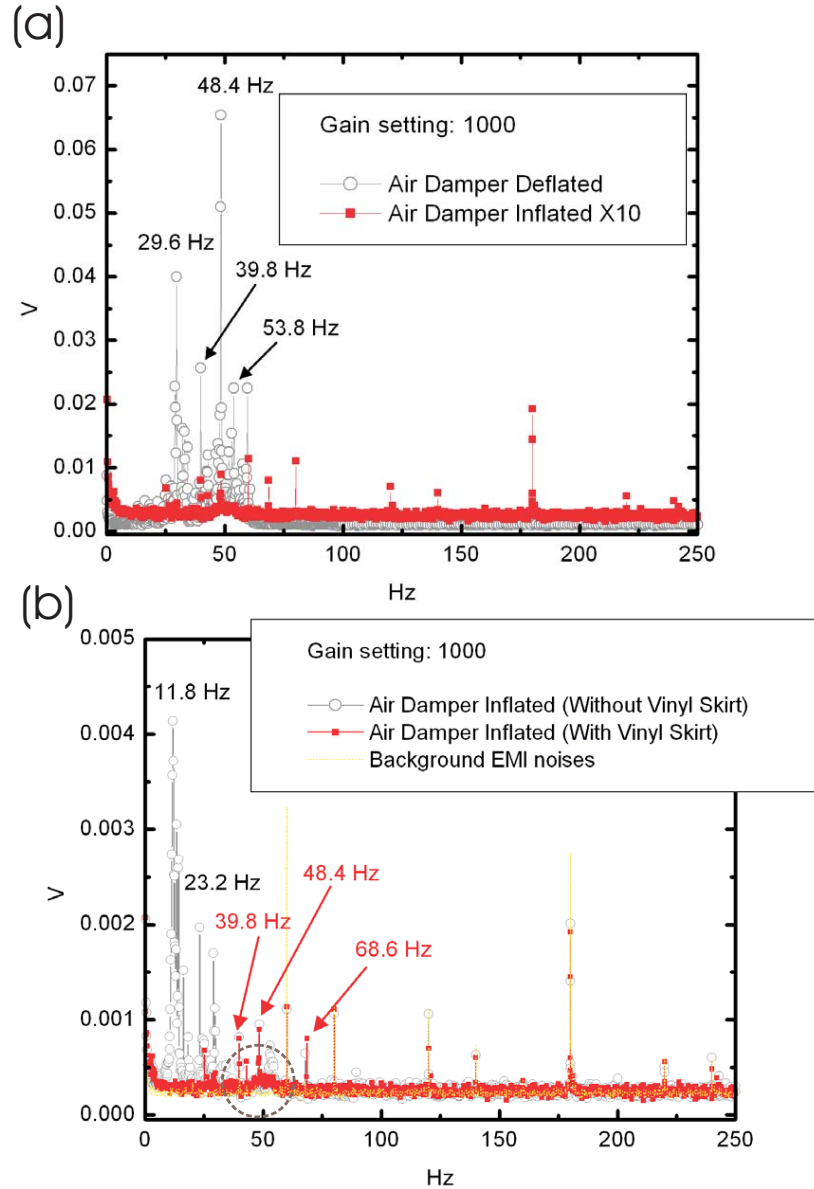


Figure 3.8: Transmitted vibrational noise spectra. (a) A comparison between noise spectrum taken with the air table deflated and that with the air table inflated. Note that the magnitude of the latter has been multiplied by 10 for clarification. The resonance modes of the building (denoted by the gray open circle), ranging from 25 – 55 Hz, are greatly suppressed when the air damper is inflated. However, there is residual spectral weight (denoted by the red solid square) centered around 50 Hz that couples to the STM probe. Noise peaks at 60, 80, 120, 140, 180, 220, and 240 Hz are line noise contaminations and Nyquist ghost artifacts, as demonstrated in (b). (b) Noise spectra taken while the air damper is inflated, with (red solid square) and without (gray open circle) the vinyl skirts attached to the edge of the table. Also shown is the noise spectrum of the background electromagnetic interference (yellow dotted line). The vinyl skirts help stabilize the air table and further reduce the low-frequency noises ranging from 5–35 Hz. Most of the remaining spectral weight is distribute around 50 Hz within the black dotted circle. For a close view of the spectrum below 150 Hz, please refer to the inset of Fig 3.9. All noise spectra are calculated by fast Fourier transforming the traces of time-varying output voltages from the piezo-electric accelerometer, ENTEK 9200L. The sensitivity of the sensor is 500 mV/g, and the sensor output is post-amplified with a gain of 1000.

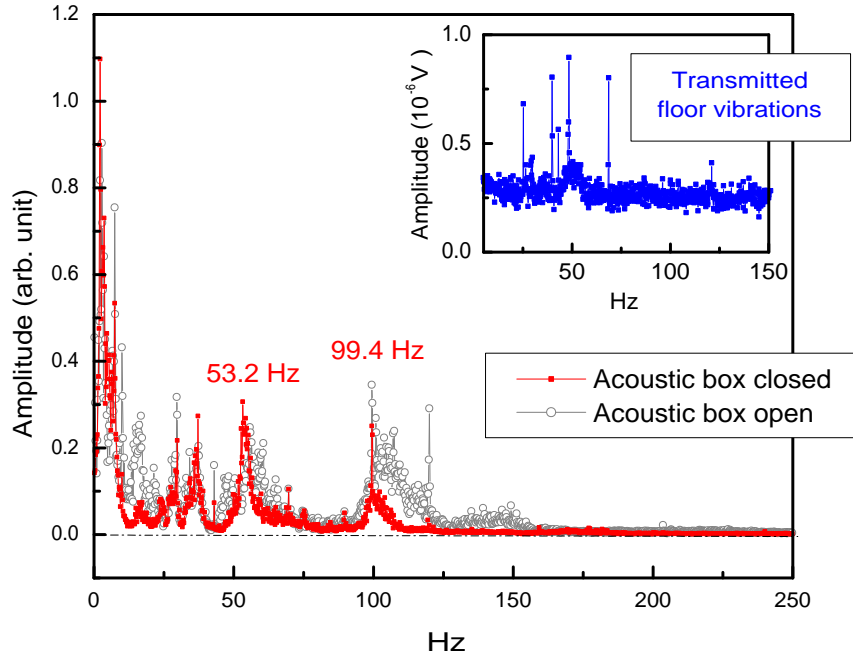


Figure 3.9: Low-frequency acoustic noise spectrum taken in the acoustic housing surrounding the STM cryostat with and without the lid closed. Above 100 Hz, the acoustic noise is mostly filtered away, while there is a substantial residual spectral weight around 50 Hz, which coincides with the residual floor vibrational noise shown in the inset.

with flat foam absorbers,¹⁷ and place crater-shaped acoustic foam above the florescent lights and the wire conduits to intercept noises rebounding from the ceiling. A bass tube¹⁸ is installed in the corner of the lab to absorb the low-frequency acoustic waves. To minimize the transmission of noise generated by the ventilation machines, rubber buffers are inserted on the pipelines connected to the side-wall. Thick vinyl curtains¹⁹ are hung in front of the entrance facing the other motor to reflect the noises, and vinyl sheets are tailored to attach to the edges of the aluminum table. These vinyl skirts keep acoustic noises from impinging upon the dewar and also provide more weight and better balance to the table. In Fig. 3.8(b), it is shown that the low-frequency vibrational noises around 12 Hz and 25 Hz are further suppressed after the installation of the skirts.

To isolate the STM system from the residual acoustic noises, a double-layer acoustic housing is built around the STM table. The inner layer is made of composite wood and the outer layer of concrete boards. Both are covered with acoustic absorption foam. The spectra of the residual

¹⁷1" thick, flat sound absorbing foam distributed by McMaster Carr.

¹⁸16" OD tube trap purchased from Silent Source.

¹⁹2 lb/ft² sound barriers from Silent Source.

acoustic noise taken via a simple microphone circuit show that the acoustic box filters away most frequencies above 100 Hz, but, around its natural frequencies, the noises are mostly transmitted [Fig. 3.9]. One of the resonant frequencies lies within 50 – 60 Hz, which coincides with the vibration frequency of the side-wall driven by the venting pipeline. Since the transmitted floor vibrations also show significant spectral weight within the same frequency range [Fig. 3.9 inset], Teflon blocks are placed irregularly between baffles to break up the resonance in order to avoid the cryogenic dewar from enhancing this mode.

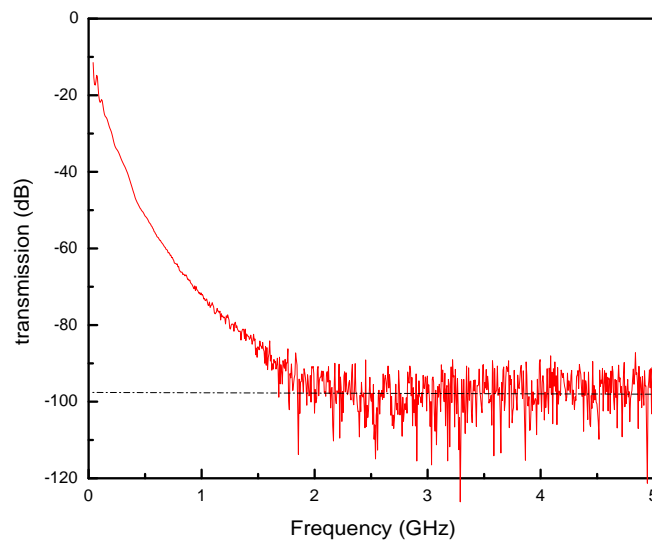


Figure 3.10: Transmission of the cryogenic microwave powder filter.

Finally, to minimize the contamination of tunneling current signals through cross-talks and environmental electromagnetic interference, we run wires of different purposes through separate thin-wall SS tubes; the latter serve as additional shielding [Fig. 3.7]. As a result, the high voltages driving the piezo-tube and shear-piezo motor are decoupled from the low-level bias voltage and the tunneling current leads. The coaxial cables carrying the bias and the tunneling signal are passed through a room-temperature RF filter²⁰ and a cryogenic powder filter²¹ [Fig. 3.10] before being connected to the STM head. To reduce the excess high-frequency noises during experiments, the high-voltage

²⁰Model BLP-1.9 from Mini-Circuits.

²¹For a brief description of the construction and modeling of cryogenic powder filters, please refer to [143].

amplifier, E-420, is turned off when coarse approach is completed and the tip is in tunneling range. Furthermore, all grounding and shielding wires are carefully arranged to avoid ground loops. After all is done, the noise floor of our system reaches about $15 - 20 \text{ pA}_{\text{p-p}}$ ($3 - 4 \text{ pA}_{\text{rms}}$) at helium temperatures.

3.3 Comparison with other experimental techniques

In this section, we briefly review other spectroscopic tools frequently applied to the study of high-temperature superconductivity.

3.3.1 Tunneling spectroscopy

Scanning tunneling spectroscopy (STS) is a local probe that measures the local density of states convoluted with the tunneling matrix element. It has superior spatial and energy resolution. On the other hand, issues such as characterizing the tip structures, preserving a good sample surface that represents the bulk properties, and determining the tunneling matrix elements can be challenging.

In addition to STS, there are several other configurations of tunnel junctions commonly seen in the high T_c community. These techniques generally sample over a much larger area than STM to yield a spatially averaged spectra. In this sense, they complement the results of STS experiments. In the following, we discuss the relative strength and the limitations of four representative tunneling techniques: planar junction spectroscopy, point contact spectroscopy, break-junction spectroscopy, and interlayer tunneling spectroscopy.

Planar junction

Planar junctions are fabricated by depositing the two electrode materials as cross strips separated by a thin layer ($\sim 10 - 40 \text{ \AA}$) of insulating material. The first N-I-S tunneling experiment [110] was carried out on planar junctions in 1960. Because of their long history, planar junctions are probably the most studied among the tunneling spectroscopy techniques. However, a number of possible pitfalls associated with these junctions have been identified, including junction contam-

ination, Coulomb blockade, Schottky barrier, heating, and barrier breakdown due to pinholes in the insulating layer. A complete set of diagnostics must be run before these potential problems can be ruled out. Schottky barrier and Coulomb blockade problems are also common for STS and point-contact spectroscopy if the sample surface has degraded. Both phenomena have distinct I-V characteristics that help identify defective junctions and avoid interpreting artifacts as real features.

In theory, one could have well-defined crystalline orientation of the thin-film samples used in the planar junctions by varying the substrate material and the growth conditions. Therefore, planar junctions have been employed to study the Andreev bound state of $\{110\}$ -oriented cuprate films [144]. However, the presence of interface roughness over a large junction area poses another complication for data analysis besides the aforementioned problems.

Point-contact spectroscopy

A point-contact is formed by pressing a sharp metallic electrode, such as Au or Pt/Ir, onto the sample of interest. By varying the spring loading applied to the tip, the tunneling barrier, and hence the junction impedance ($\sim 1\Omega - 1k\Omega$), can be adjusted to probe the conductance spectrum from the point-contact limit to near the tunneling limit. Compared to STM, point-contact experiments are much easier to set up for variable temperature and variable magnetic field measurements. In addition, they do not have the problem of pinholes or shorts through the insulating layer as in the planar junctions. However, the preparation for a clean tip and a good sample surface is non-trivial. The large springing force needed to form a good contact also poses a problem for maintaining the sample surface integrity and the mechanical stability of the system. A recent review of the application of point-contact spectroscopy to studies of the Andreev process in cuprate superconductors can be found in an article by Deutscher [145].

Break-junction

In a break-junction setup, a thin piece of sample is glued to a flexible support. By carefully bending the support, the sample is broken into two pieces, and, by slowly reducing the stress, the two parts are brought back to establish a tunnel junction. Compared with planar junctions and

point-contact spectroscopy, break junctions have the advantage of retaining fresh junction surfaces because the junctions are generally formed in vacuum at cryogenic temperatures. The down side is that the intrinsic randomness in the break surface and the reformation process renders it almost impossible to control the orientations of the junction electrodes. Thus, it is not a good choice for measuring orientation-dependent properties, such as tunneling into the Andreev bound states.

Break junctions on the nearly two-dimensional Bi-2212 samples have been prepared in two different ways. One is by applying the bending method as mentioned above to fabricate in-plane tunnel junctions [146]. The other method takes advantage of the extremely weak bonding between BiO₂ planes to form *c*-axis tunnel junctions. By pushing a sharp tip into the sample and subsequently releasing the pressure, a fracture between planes is formed about 100 μm below the surface [147]. Therefore, the junction is pristine and free of surface contaminations. Spectra taken on *c*-axis break junctions of Bi-2212 in the superconducting state have revealed a pronounced “peak-dip-hump” feature [147, 148, 149] consistent with the photoemission spectra on similar samples. We shall return to discuss the physical origin of the “peak-dip-hump” feature in later chapters.

Interlayer tunneling spectroscopy

Interlayer tunneling spectroscopy is also referred to as the intrinsic Josephson tunneling because it makes use of the extreme two dimensionality of certain cuprates, *e.g.*, Bi-2212, and measures their *c*-axis interlayer tunneling spectra. To avoid the complication in the interpretation of data, the sample thickness is controlled to contain less than 25 Josephson junctions. With the advance in fabrication technology, several groups [150, 69] have demonstrated the ability to reliably fabricate Bi-2212 mesas with as few as 9 Josephson junctions, corresponding to a thickness of ~ 15 nm. Like the break junctions, interlayer Josephson junctions are free of junction contaminations. Furthermore, the junction orientation is well-defined along the *c*-axis, and, therefore, it would appear to be the best configuration to study the *c*-axis tunneling of highly 2D Bi-2212 and Bi-2201 samples. Indeed, earlier intrinsic tunneling spectra on Bi-2212, which exhibited coexisting pseudogap and superconducting gap with disparate temperature evolutions [69, 151, 152], have drawn wide attention and intensified the debate of how pseudogap phase relates to high-temperature superconductivity.

However, the interpretation of the spectra is not without dispute. For instance, due to the poor thermal conductivity of Bi-2212, joule-heating has always been a main concern for possibly giving rise to non-intrinsic phenomena observed in the Bi-2212 mesas [153, 154]. Experimental efforts to reduce or calibrate away the effect of joule-heating include the use of short duty-cycle pulse measurements [155], the on-chip thermometry [156, 154], and the *in situ* temperature control [157].

3.3.2 Angle-resolved photoemission spectroscopy

Angle-resolved photoemission spectroscopy (ARPES) measures the single-particle spectral function. By shining a beam of monochromatized radiation (usually in the ultra-violet range) on a well-aligned single crystal sample, valence electrons are excited and escape into vacuum via the photoelectric effect. By analyzing the energy and angular distribution of the photoelectrons, the spectral function (convoluted with the one-electron dipole matrix element and the Fermi function) is derived. The spectral function $A(\vec{k}, \omega)$ is related to the retarded Green's function by the expression

$$A(\vec{k}, \omega) = -\frac{1}{\pi} \text{Im} G^{\text{ret}}(\vec{k}, \omega), \quad (3.1)$$

where $G^{\text{ret}}(\vec{k}, \omega)$ is the momentum-space Fourier transform of the real-space retarded Green's function $G^{\text{ret}}(\vec{r}, \vec{r}, \omega)$.²² Careful analysis of the ARPES spectra can yield information on the electron proper self-energy, $\Sigma(\vec{k}, \omega) = \Sigma'(\vec{k}, \omega) + \Sigma''(\vec{k}, \omega)$,

$$A(\vec{k}, \omega) = -\frac{1}{\pi} \frac{\Sigma''(\vec{k}, \omega)}{(\omega - e_k - \Sigma'(\vec{k}, \omega))^2 + (\Sigma''(\vec{k}, \omega))^2}. \quad (3.4)$$

The self-energy $\Sigma(\vec{k}, \omega)$ describes the energy renormalization and the finite lifetime of the quasiparticles, which serves as a useful comparison to other techniques that measure the scattering rate and

²²Let H be the total Hamiltonian of the system and $\psi_{\mathbf{q}}(\vec{r})$ the single-particle eigenstates. Then $G^{\text{ret}}(\vec{r}, \vec{r}, t)$ is defined as:

$$G^{\text{ret}}(\vec{r}, \vec{r}, t) = -i\theta(t) \sum_{\mathbf{q}} \langle \vec{r} | e^{-i\hat{H}t/\hbar} | \psi_{\mathbf{q}} \rangle \langle \psi_{\mathbf{q}} | \vec{r} \rangle = -i\theta(t) \sum_{\mathbf{q}} \langle \vec{r} | e^{-i\omega_{\mathbf{q}}t/\hbar} | \psi_{\mathbf{q}} \rangle \langle \psi_{\mathbf{q}} | \vec{r} \rangle \quad (3.2)$$

and thus

$$G^{\text{ret}}(\vec{r}, \vec{r}, \omega) = \sum_{\mathbf{q}} \frac{|\psi_{\mathbf{q}}(\vec{r})|^2}{\omega - \omega_{\mathbf{q}} + i\delta}. \quad (3.3)$$

the relaxation rate.

Scanning tunneling spectroscopy and ARPES are complementary techniques in that STS measures local spectral function $N_s(\vec{r}, \omega)$ with high spatial resolution, while ARPES measures the spectral function $A(\vec{k}, \omega)$ with momentum resolution. It is worth noting that the angular resolution in ARPES comes at a price of reduced energy resolution [158]. Over the past decade, there has been an order-of-magnitude improvement in the energy resolution of ARPES to $\sim 5\text{meV}$. However, it is still far behind what STS could provide.

To ensure the best momentum and energy resolution, ARPES on cuprate material generally works at lower photon energies (20 – 100 eV). Consequently, the mean free path for ballistic photoelectrons is on the order of 5\AA , rendering ARPES extremely surface sensitive. To date, most of ARPES data on the cuprates have been taken on highly 2D samples because they could be easily cleaved to yield good surfaces. In particular, the ARPES data of the Bi-2212 families are among the most complete. It is known from STS measurements [67, 68] that Bi-2212 reveals strong spatially varying tunneling spectra possibly due to inhomogeneous interstitial oxygen doping and competing order. On the other hand, ARPES averages over electrons ejected from a macroscopic area illuminated by the incoming photon beam. Thus, one must keep in mind that ARPES data as well as other bulk measurements on Bi-2212 present averaged information.

ARPES has been widely used by the high T_c community as means to survey the normal state properties, identify the Fermi surfaces, investigate the anisotropy of superconducting gap and pseudogap, and study the evolution of spectral function from below to above T_c . A comprehensive review on the recent progress can be found in Ref. [158]. In later chapters, we will draw on two ARPES observations, the peak-dip-hump structure [159] and the dichotomy between nodal and anti-nodal quasiparticle spectra in the pseudogap phase [160], and discuss how these novel phenomena relate to our STS results.

3.3.3 Neutron scattering

The proximity of cuprate superconductors to the anti-ferromagnetic Mott insulating phase gives rise to several interesting magnetic orders in cuprate systems. The studies of the doping-dependent magnetic properties can conceivably lead to important insight into the underlying pairing mechanism of cuprate superconductors. Neutron scattering has been the most widely used spectroscopic technique to investigate the dynamic and static magnetic correlations of cuprates by the high T_c community. Because neutrons are charge neutral, they interact weakly with the system under study, penetrate much deeper into the sample, and thus allow the bulk magnetic properties of sample to be explored. On the other hand, the weak interaction renders scattering cross sections small. Thus, high quality cm^3 size crystals are generally required to overcome the instrumentation noises. As a result, only two families of cuprates, $\text{La}_{2-x}\text{Sr}_x\text{CuO}_4$ and $\text{YBa}_2\text{Cu}_3\text{O}_{6+\delta}$, have been studied in detail to date.

Neutron scattering data contain contributions from both the phonon modes and the magnetic fluctuations. Because of the difference in the form factors, it is possible to distinguish magnetic scattering from phonon scattering by probing the angular dependence of the scattering cross section. In addition, polarized neutron scattering can be employed to filter out the phonon spectral weight completely. However, the signals of the polarized neutron scattering configuration are substantially smaller than those of the unpolarized configuration, and thus extracting signals from background noises can be very challenging for the polarized neutron scattering experiments.

Inelastic neutron scattering measures the dynamic scattering cross section, which is proportional to the dynamic structure factor and hence to the imaginary part of the generalized susceptibility:

$$\frac{\partial^2 \sigma}{\partial \Omega_f \partial E_f} \sim \left| f(\vec{Q}) \right|^2 \frac{|\vec{k}_f|}{|\vec{k}_i|} \sum_{\alpha, \beta} (\delta_{\alpha\beta} - \hat{Q}_\alpha \hat{Q}_\beta) S^{\alpha\beta}(\vec{Q}, \omega) \quad (3.5)$$

$$S^{\alpha\beta}(\vec{Q}, \omega) = \frac{1}{1 - e^{-\hbar\omega/kT}} \text{Im} \chi(\vec{Q}, \omega), \quad (3.6)$$

where $\vec{Q} = \vec{k}_f - \vec{k}_i$ and $f(\vec{Q})$ is the form factor. The elastic neutron scattering experiments measure the magnetic Bragg scattering from the sample, which can reveal long-range magnetic structures

such as the stripe order in $\text{Nd} - \text{La}_{2-x}\text{Sr}_x\text{CuO}_4$ [84] and the anti-ferromagnetic order in the undoped cuprate compounds [chap:introduction]. In fact, neutron scattering was the first technique to demonstrate the anti-ferromagnetic spin configurations of the undoped parent compounds [1], disproving the conjecture of a resonating-valence-bond spin liquid phase as the ground state for the undoped cuprates [20]. Comprehensive reviews on the earlier neutron scattering results of $\text{La}_{2-x}\text{Sr}_x\text{CuO}_4$ and $\text{YBa}_2\text{Cu}_3\text{O}_{6+\delta}$ can be found in Refs. [2, 161, 162, 163, 164].